

Solar Thermochemical Redox Cycling Using Ga- and Al-Doped LSM Perovskites for Renewable Hydrogen Production

Dylan C. McCord, Elizabeth J. Gager, Ximeng Wang, Taylor L. Johnson, Jonas S. Beachy, Keith A. King, Simon R. Phillipot, Juan C. Nino, Anthony H. McDaniel, and Jonathan R. Scheffe*



Cite This: *J. Phys. Chem. C* 2024, 128, 15796–15806



Read Online

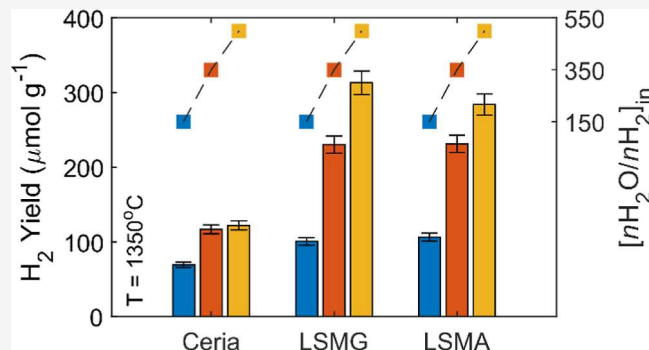
ACCESS |

Metrics & More

Article Recommendations

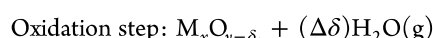
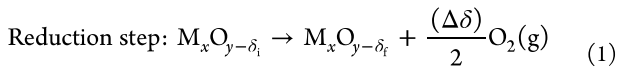
Supporting Information

ABSTRACT: Solar thermochemical hydrogen production using redox-active metal oxides is a promising pathway for the production of green hydrogen and synthetic fuel precursors. Herein, the perovskite material $(\text{La}_{0.6}\text{Sr}_{0.4})_{0.95}\text{Mn}_{0.8}\text{Ga}_{0.2}\text{O}_{3-\delta}$ (LSMG6482) is identified as a promising metal oxide for thermochemical water splitting. LSMG6482, along with more-established water splitters ceria and $(\text{La}_{0.6}\text{Sr}_{0.4})_{0.95}\text{Mn}_x\text{Al}_{1-x}\text{O}_{3-\delta}$ (LSMA) perovskites, is experimentally characterized via thermogravimetric (TGA) analysis and high-temperature water splitting in a reactor simulating solar concentrating conditions. TGA analysis demonstrated that LSMG6482 has high and stable oxygen exchange capacity under controlled $p\text{O}_2$ redox cycling, demonstrated by large changes in oxygen nonstoichiometry (δ) relative to ceria. Water splitting experiments using laser heating ($T_{\text{red}} = 1400^\circ\text{C}$, $T_{\text{ox}} = 1200^\circ\text{C}$) resulted in H_2 yields of $165.1 \mu\text{mol g}^{-1}$ for the candidate LSMG6482 composition, exceeding that of all benchmark materials tested. Under high conversion oxidation conditions, where H_2 is cointroduced with H_2O ($150 \leq n\text{H}_2\text{O}/n\text{H}_2 \leq 500$), H_2 yields were greatest for LSMG6482 and LSMA6482, up to four times that of ceria at the highest $n\text{H}_2\text{O}/n\text{H}_2$ conditions. Crystallographic analysis showed that over the course of experimentation, there is some secondary phase growth for all perovskite compositions, except for LSMA6482, but there was no observable degradation in H_2 yields.



INTRODUCTION

Thermochemical redox cycling of metal oxides is a promising pathway to split water and produce green H_2 . In this process, a redox-active metal oxide (typically a nonstoichiometric oxide, denoted here as $\text{M}_x\text{O}_{y-\delta_i}$) is reduced at high temperature using concentrated solar energy to drive the endothermic reduction of the metal oxide and release gaseous oxygen, as shown in eq 1. δ is the oxygen nonstoichiometry, subscripts i and f refer to the initial and final values, and $\Delta\delta$ is the change in the oxygen nonstoichiometry of the reaction. In a subsequent oxidation step, shown in eq 2, H_2O reacts with the reduced oxide to produce H_2 . The magnitude of the δ terms of the metal oxide at a given reduction temperature (T_{red}), oxidation temperature (T_{ox}), and oxygen partial pressure ($p\text{O}_2$) is ultimately dictated by the thermodynamic properties of the metal oxide, namely, the partial molar change in enthalpy and entropy during oxygen exchange.¹



Nonstoichiometric cerium dioxide ($\text{CeO}_{2-\delta}$), or ceria, is regarded as the state-of-the-art metal oxide for two-step thermochemical cycling.^{2,3} Ceria possesses desirable thermodynamic and kinetic properties for water splitting cycling while maintaining excellent chemical stability in its cubic fluorite structure.^{4–6} However, in order to achieve a large potential for oxidation (i.e., sufficient δ_f), reduction at high temperatures is necessary because of its high oxygen vacancy formation energy. The oxidation step is typically performed at a lower temperature and consequently lower $p\text{O}_2$ ($\leq 1000^\circ\text{C}$, 10^{-20} atm $< p\text{O}_2 < 10^{-10}$ atm) where oxidation is more thermodynamically favorable.³ While the oxidation reaction

Received: April 29, 2024

Revised: August 21, 2024

Accepted: August 23, 2024

Published: September 17, 2024

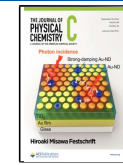


Table 1. Materials and Relevant Dimensions^a

chemical formula	abbreviation	TGA structure	TGA mass (g)	SFR structure	SFR mass (g)
(La _{0.6} Sr _{0.4}) _{0.95} (Mn _{0.8} Ga _{0.2})O _{3-δ}	LSMG6482	pellet (200 μm, 400 μm)	0.103, 0.203	Powder	0.105
(La _{0.6} Sr _{0.4}) _{0.95} (Mn _{0.8} Al _{0.2})O _{3-δ}	LSMA6482	pellet (200 μm, 400 μm)	0.094, 0.189	Powder	0.102
(La _{0.6} Sr _{0.4}) _{0.95} (Mn _{0.6} Al _{0.4})O _{3-δ}	LSMA6464	pellet (200 μm, 400 μm)	0.086, 0.188	Powder	0.077
(La _{0.6} Sr _{0.4}) _{0.95} (Mn _{0.4} Al _{0.6})O _{3-δ}	LSMA6446	pellet (200 μm, 400 μm)	0.115, 0.199	Powder	0.100
CeO _{2-δ}	ceria	pellet (200 μm, 400 μm)	0.109, 0.218	Powder	0.102

^aAll thermogravimetry experiments were performed with pellets of thicknesses 200 μm and 400 μm and diameter of 12.7 mm. All flow reactor experiments were performed using powders.

typically occurs at these lower oxygen partial pressures, it should be noted that this is simply a thermodynamic result of operating at lower temperatures, but increasing the oxygen partial pressure during oxidation will certainly benefit the reaction. The magnitude of the temperature swing between T_{red} and T_{ox} is especially relevant to the overall efficiency due to the large sensible heating demands.⁷ To date, the highest solar-to-fuel efficiencies have been achieved by Zoller using a 50 kW solar reactor during CO₂ splitting cycles rather than H₂O to obtain an efficiency of 5.60% and by Marxer et al. using a 4 kW solar reactor during CO₂ splitting cycles to obtain an efficiency of 5.25%.^{8,9} The majority of the irreversibility in the latter was due to solid's heating between T_{red} and T_{ox} .

Perovskite metal oxides, having the form ABO_{3-δ}, have been identified as a material class with favorability toward reduction at lower T_{red} , thus potentially overcoming a major source of sensible heating demand present in cycling with ceria. Perovskites present a large space for material discovery of highly efficient water splitting materials due to the tunability of their thermodynamic properties through doping of the A and B lattice sites.¹⁰ The perovskite material space has been probed for efficient redox materials, with some success over the past decade. Sr-doped lanthanum manganites (LSM) proposed by Scheffe et al.¹¹ and Sr- and Al-doped LaMnO₃ (here presented as LSMA) proposed by McDaniel et al.^{12,13} both demonstrate a propensity to produce H₂ at lower temperature reduction conditions compared to ceria. Ezbiri et al. probed the effects of changing A-site and B-site cation ratios on the LSMA system, finding that increasing Sr-doping on the A-site resulted in an increase in the reduction extent, while changing B-site doping ratios had little effect on the reduction extent.¹⁴ More recently, it was shown by Şanlı and Pişkin that when holding A-site ratios constant, increasing Al content on the B-site results in an increase in the reoxidation capacity.¹⁵ Further LSMA doping schemes were investigated by Deml et al. through density functional theory (DFT) and thermogravimetric (TGA) efforts, identifying LSMA6464 as the optimal dopant concentration.¹⁶ The thermodynamic properties of the LSMA system, namely partial molar enthalpy and entropy, were characterized Cooper et al., Ezbiri et al., and Takacs et al., finding that the partial molar changes in enthalpy during oxygen exchange using LSMA was significantly lower than that of ceria, resulting in lower temperature reductions.^{17–19} Using these properties, Carrillo and Scheffe¹ predicted that these perovskite classes can potentially have higher solar-to-fuel efficiencies than ceria if operated isothermally (i.e., $T_{\text{red}} \sim T_{\text{ox}}$) or near isothermally with high oxidant delivery (i.e., low H₂O conversion) and sufficient gas phase heat recovery. In a similar study, Muhich et al. reached similar conclusions that in order for viable operation of LSM-type systems, operating strategies must prioritize gas to gas heat recuperation due to the low H₂O conversions at the conditions where the perovskites best

perform.²⁰ Such high-temperature oxidizing conditions were shown to be experimentally viable by Muhich et al. using a hercynite cycle, by Hao et al. using ceria, and by Lee et al. using the perovskite (La_{0.65}Sr_{0.35})_{0.95}MnO₃ (LSM35).^{21–23} It should be noted, however, that with high-temperature oxidations and excess oxidant delivery, it is expected that there may be some water thermolysis resulting in a mixture of O₂ in the H₂ gas product that may require downstream separation. The LSM-system was further investigated by Dey et al. by doping the B- site with Al, Ga, or Sc, which were chosen because of their similar desirable conductivity properties.²⁴ They found that the CO yields during the CO₂ splitting cycles were enhanced most by Sc, followed by Ga, then Al. New developments of the perovskite class also include the development of high-entropy perovskite oxides with complex A-sites, which have emerged in more recent studies, demonstrating their applicability to solar thermochemical hydrogen (STCH) technology.²⁵ Overall, recent developments of perovskites for thermochemical cycling has involved a refinement of doping strategies in part driven by computation such as that presented by Emery et al. where 383 potential compounds were identified.²⁶

Recent computational work from Wang et al.²⁹ revealed that B-site Ga- and Al-doped LSM perovskites possess desirable oxygen vacancy formation energy (E_v^0) for STCH applications. The computational results for Al-doped LSM are supported by the vast amount of literature discussed above. However, Ga-doped LSM has been investigated only under a limited number of CO₂ splitting conditions. Namely, Dey et al.²⁴ demonstrated temperature swing CO₂ cycling but under conditions of excess CO₂ (i.e., 40% in Ar) and under a 300 °C temperature swing and only three cycles. The impact of operating under more realistic, high conversion gas splitting conditions (i.e., CO in CO₂ or H₂ in H₂O) was not tested or compared to the state-of-the-art ceria, and the thermodynamic properties, which are important for process modeling, have not been measured (i.e., bulk oxygen capacity as a function of temperature and pO₂). Further, the viability of gas splitting has not been tested under isothermal or near-isothermal conditions, where LSM-based perovskite compositions are likely to have a competitive thermodynamic advantage compared to the state-of-the-art ceria.²¹ Therefore, the goal of this work is to study the LSMG perovskite under more extensive conditions to help provide a comprehensive understanding of the water splitting capability of Ga-doped LSM and place its performance among more notable, well-understood water splitting candidates, namely, ceria, LSMA6464 and LSMA6446 (two of the best-performing Al-doped LSM perovskites from the literature discussed above), and LSMA6482, a direct analogue to the primary doping scheme of LSMG investigated herein. Ceria and the Al-doped LSM perovskites are subjected to a series of experiments

alongside LSMG to serve as benchmarks for STCH performance. The candidates were initially subjected to TGA characterization to quantify equilibrium oxygen nonstoichiometry at high temperatures and high oxygen partial pressures (in the range where reduction and high temperature oxidation are expected to occur, i.e., near isothermal conditions). Subsequent water splitting experiments were performed under simulating solar concentrating conditions with a temperature swing of $\Delta T = 200\text{ }^{\circ}\text{C}$ and under high conversion conditions (mixtures of H_2O and H_2) to better understand the dynamics in scaled-up systems. Crystallographic analysis is presented of the as-synthesized and postcycled material compositions.

■ EXPERIMENTAL SECTION

Ceramic Synthesis. Materials used throughout this work are listed in Table 1. Other Ga dopant concentrations were considered only for select water splitting experiments, with the results discussed in “Water Splitting Capability”. Pellets were used in TGA experiments that varied in thickness to probe transport limitations, if any, which are relevant to future kinetic-specific studies. Perovskite compositions were synthesized via a solid-state method. Powdered samples were synthesized from La_2O_3 (99.99%, Cerac), SrCO_3 (>99.9%, Sigma-Aldrich), MnO_2 (99.99, Acros Organics), and either Ga_2O_3 (99.999%, Alfa Aesar) or Al_2O_3 (99.995%, Alfa Aesar). La_2O_3 was heated to $900\text{ }^{\circ}\text{C}$ for 1 h prior to synthesis to ensure decomposition of lanthanum hydroxide, and all other precursors were dried overnight at $120\text{ }^{\circ}\text{C}$ prior to use. Stoichiometric amounts of precursors were mixed using a unitary ball mill with yttria-stabilized zirconia media for 20 h. After mixing, the mixture was dried, and the powders were calcined at $1200\text{ }^{\circ}\text{C}$ for 4 h. For the pelletized samples, following calcination, the powder was uniaxially pressed at approximately 150 MPa into 0.5 g cylindrical pellets, 12.7 mm in diameter using 1 wt % polyvinyl alcohol (PVA) binder. The pressed pellets had geometrical density values between 50 and 60% compared to those of a fully dense pellet. The pellets were heat treated with a binder burnout step at 450 and $600\text{ }^{\circ}\text{C}$ for 2 and 4 h, respectively. Then, the pellets were sintered using a two-step profile with $T_1 = 1300\text{ }^{\circ}\text{C}$ and $T_2 = 1030\text{ }^{\circ}\text{C}$ with 30 min and 10 h hold times. The pellets were then annealed at $1450\text{ }^{\circ}\text{C}$ for 6 h. After annealing, the pellets were polished to the desired thickness. Commercial ceria powder (99.9%, Sigma-Aldrich) was used as received. Ceria pellets were sintered at $1650\text{ }^{\circ}\text{C}$ for 2 h and polished to 200 and $400\text{ }\mu\text{m}$ thicknesses.

Crystallographic Characterization. X-ray diffraction (XRD) data were collected from powders and pellets before and after cycling experiments using the conventional Bragg–Brentano θ – 2θ diffractometer configuration (Panalytical XPert Powder). Characterization was performed using a Cu X-ray source with a voltage of 45 kV, step size of 0.016° , dwell time of 10 s, current of 40 mA, and 2θ value of 20 – 70° .

TGA Characterization. TGA analysis of pelletized samples was performed with a Mettler Toledo TGA (HT TGA/DSC 2). The TGA afforded precise temperature control and atmospheric control of $p\text{O}_2$ by mixing of prescribed trace oxygen mixtures and argon using the equipped Mettler Toledo gas controller (GC 200). $p\text{O}_2$ was monitored throughout the entirety of each experiment using a zirconia-probe-based oxygen sensor (Econox CarboProbe DS). The mass data gathered from the TGA screenings were used to characterize

redox behavior in terms of δ and $\Delta\delta$ through the relationship shown in eq 3.

$$\delta_t = \frac{m_s - m_t}{m_s} \frac{M_s}{M_O} \quad (3)$$

here, δ_t is the instantaneous oxygen nonstoichiometry of the sample and m_t is the instantaneous mass of the sample. m_s is the stoichiometric mass of the sample or the mass at $\delta = 0$. M_s and M_O are the molar masses of the sample and monatomic oxygen, respectively. Pelletized discs (100–200 mg depending on the thickness of the sample) of each composition were placed in a platinum crucible and subjected to several isothermal redox cycles at temperatures ranging from 1200 to $1400\text{ }^{\circ}\text{C}$.

TGA experiments were split into two methods to facilitate the limited range of $p\text{O}_2$ accessible when using trace oxygen mixtures. The first method, at the low oxygen partial pressure range, began with a $20\text{ }^{\circ}\text{C}/\text{min}$ ramp to $1000\text{ }^{\circ}\text{C}$ where the material dwelled for 30 min and allowed the system to equilibrate at the higher temperature under the reduction gas (pure Ar) with a background $p\text{O}_2$ of $10^{-3.94}$ atm. The temperature was then increased to the first set point and allowed to reach full equilibrium, indicated by a steady mass signal from the TGA. Upon equilibrium, $p\text{O}_2$ was stepwise increased to $10^{-3.41}$ atm, referred to as oxidation 1, and was again allowed sufficient time to reach equilibrium. $p\text{O}_2$ was then reversed back to the prior reduction conditions. Following equilibrium at reduction, $p\text{O}_2$ was stepwise increased to $10^{-3.30}$ atm, referred to as oxidation 2, and then reversed to the prior reduction conditions again. The temperature was then increased to the next set point, and the procedure was repeated. Following cycling at the last temperature, the sample temperature was decreased to $1000\text{ }^{\circ}\text{C}$ at which point a mixture of 33% O_2 balanced in Ar was introduced to fully oxidize the sample and obtain a value for m_s . The second method was performed similarly, with $p\text{O}_2$ values of $10^{-3.61}$, $10^{-3.05}$, and $10^{-2.94}$ atm for reduction, oxidation 1, and oxidation 2, respectively. Dynamic environment effects during gas switching and temperature changes were accounted for by blank subtraction.

Water Splitting Methodology. Samples were subjected to three temperature swing water splitting cycles in the Sandia National Laboratory (SNL) stagnation flow reactor (SFR). Capabilities and detailed description of the SFR are described elsewhere.^{12,27,28} Briefly, the SFR utilizes a vertically oriented Carbolite tube furnace to control the temperature within the concentric reaction tubes that are suspended in the hot zone of the furnace. The reaction tube is topped with a 500 W continuous-wave near-infrared laser coupled with a pyrometer to afford rapid concentrated heating and reduction temperature control. Steam, argon, and other reactive gases are delivered via mass flow controllers, leading to the inlet of the reaction tube. At the exit of the reaction tube, water is condensed out of the gas stream in cryogenic chillers, and noncondensable product gas is measured in a mass spectrometer. The total pressure of the system is held nominally at 76 Torr.

Fresh powder samples of approximately 100 mg each were subjected to a laser-driven temperature swing cycle between reduction temperature $T_{\text{red}} = 1400\text{ }^{\circ}\text{C}$ and oxidation temperature $T_{\text{ox}} = 1200\text{ }^{\circ}\text{C}$. Each experiment began with a three-point calibration, in addition to one zero point of the

hydrogen signal from the mass spectrometer against known hydrogen flow rates. After calibration, the temperature in the tube furnace was increased to T_{ox} at a rate of 10 °C/min under 25% O₂ balanced in Ar. Once T_{ox} was reached, the system was purged with pure argon for 20 min resulting in a background $p\text{O}_2$ of $\sim 10^{-5.96}$ atm. Reduction was then initiated by laser heating and was allowed to proceed for 330 s. The laser heating was then stopped, allowing the sample temperature to cool to T_{ox} . The system was then purged with argon for 300 s to sweep out any excess oxygen before adding 200 sccm of steam to the argon flow for 1300 s to drive the oxidation at a $p\text{O}_2$ of $10^{-5.07}$. Again, argon was used to purge the system for 300 s, and the cycle was repeated. Three temperature swing cycles were performed following this procedure for each sample. Thermolysis and gas changing effects were accounted for through blank subtraction.

High conversion cycling behavior (i.e., cycling in a reactive gas stream that has been diluted with product gas) was also characterized in the SFR at temperatures ranging from 1300 to 1400 °C. Samples were reduced at temperatures between 1300 and 1400 °C and fixed $p\text{O}_2$ of $10^{-6.5}$ atm (set by controlling $[n\text{H}_2\text{O}/n\text{H}_2]_{\text{in}}$), for sufficient time to allow the reaction to equilibrate (i.e., no predetermined reaction time). Then, oxidation was initiated by stepwise increasing the H₂O flow rate such that $[n\text{H}_2\text{O}/n\text{H}_2]_{\text{in}}$ was increased. The oxidation reaction, characterized by a net production of H₂, was given sufficient time to equilibrate, as indicated by a return of the hydrogen signal to the baseline. Then, the process was repeated, whereby the reduction reaction was initiated by again decreasing $[n\text{H}_2\text{O}/n\text{H}_2]_{\text{in}}$, followed by oxidation and so on. The method was conducted for oxidation conditions of $[n\text{H}_2\text{O}/n\text{H}_2]_{\text{in}} = 300, 400,$ and 500 at 1300 °C, $[n\text{H}_2\text{O}/n\text{H}_2]_{\text{in}} = 150, 350,$ and 500 at 1350 °C, and $[n\text{H}_2\text{O}/n\text{H}_2]_{\text{in}} = 150, 350,$ and 400 at 1400 °C.

RESULTS AND DISCUSSION

Dopant Selection Motivation (E_v^{O}). In prior work, Ga and Al were found to be suitable B-site dopants on the LSM perovskite due to promising E_v^{O} .²⁹ The methods and results are presented in detail by Wang et al. and are summarized here in the context of active water splitting experiments. To summarize results related to this work, A-site dopants of Ca and Sr were found to exhibit the full range of E_v^{O} and thermodynamic stability in the relevant redox condition range (2.5–4.0 eV), while on the B-site, Al and Ga doping resulted in thermodynamic stability in the temperature and $p\text{O}_2$ range of interest and oxygen vacancy formation energies in the target range. Specifically, Ga-doping resulted in E_v^{O} of 3.5–4 eV and Al-doping resulted in E_v^{O} of 3.6–4.2 eV. Promising results were also observed for Zn and Mg doping on the B-site but were not considered for synthesis due to volatility concerns. A-site Sr doping and B-site Al doping results in a well-established water splitting material (LSMA), validating these computational results, and has been studied and characterized in great detail.^{12,17,18} Thus, this makes it an excellent benchmark material for comparison to other LaMnO₃ doping schemes. Ga-doping on the B-site with Sr on the A-site has only briefly been explored by Dey et al.,²⁴ motivating further investigation in this work.

Bulk Oxygen Behavior—Oxidation Conditions. Select TGA results and the corresponding temperature and $p\text{O}_2$ for the pelletized perovskites and ceria are shown in Figure 1. Here, it is shown that each material is capable of reversibly

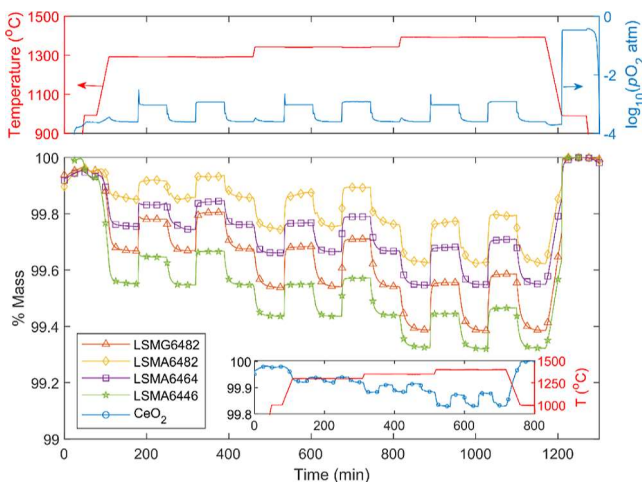


Figure 1. Top: Measured temperature and $p\text{O}_2$. Bottom: TGA measurements of percent mass change for LSMG6482, LSMA6482, LSMA6464, LSMA6446, and ceria in a trace oxygen atmosphere. Ceria is shown inlaid in the bottom plot, subjected to the same conditions on a different timescale. Here, the 400 μm thick pellets were used and $p\text{O}_2$ ranged from $10^{-3.61}$ to $10^{-2.94}$ atm.

transporting oxygen in and out of its lattice between 1300 and 1400 °C. In this data set, $p\text{O}_2$ was varied between $10^{-3.61}$, $10^{-3.05}$, and $10^{-2.94}$ atm, but wider ranges are measured and presented in the subsequent Figure 2. As expected, all materials

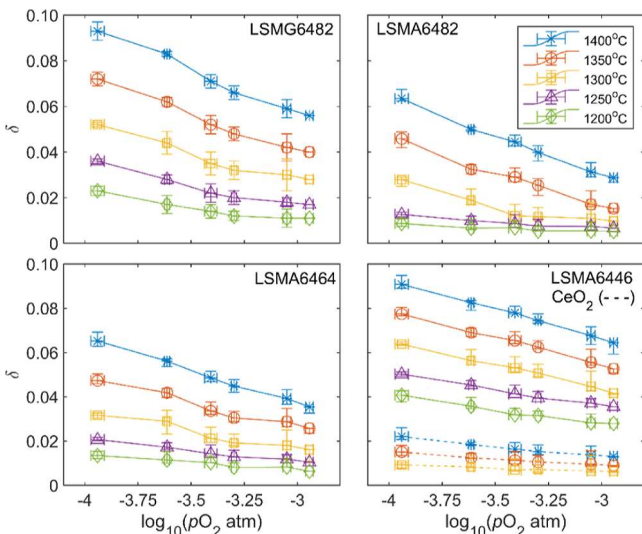


Figure 2. Equilibrium oxygen nonstoichiometry for LSMG6482, LSMA6482, LSMA6464, LSMA6446, and ceria as a function of temperature and oxygen partial pressure. Perovskites are shown as solid lines, and ceria is shown as a dotted line. Error bars represent 2σ from the measured average.

responded to a decrease in $p\text{O}_2$ at constant temperature with a decrease in mass due to oxygen evolution, while an increase in $p\text{O}_2$ at constant temperature resulted in an increase in mass due to oxygen uptake. Similarly, when temperature was increased at a constant $p\text{O}_2$, all materials responded with a mass decrease due to oxygen evolution, while decreasing the temperature at a constant $p\text{O}_2$ resulted in an increase in mass due to oxygen uptake. At each condition, the materials were given 70 min to reach equilibrium, indicated by stabilization of the mass signal. Stoichiometric mass was indexed at 1000 °C in

a 33% O₂/Ar atmosphere, where all released oxygen was recovered by the material, indicated by a return to the starting mass.

Experiments such as the one shown in Figure 1 were repeated and extended to a larger range of temperatures and pO₂. The total extent of the results is mapped into the δ space and is shown in Figure 2. Here, isotherms from 1200 to 1400 °C for each material are presented as a function of pO₂ between 10^{-3.94} and 10^{-2.94} atm. The asterisks are an average of equilibrium measurements for δ at each condition, connected linearly between each condition to illustrate the general shape of each isotherm. Vertical and horizontal error bars represent average $\delta \pm 2\sigma_\delta$ and average $pO_2 \pm 2\sigma_{pO_2}$, respectively. Ceria mass changes approached the resolution limit of the experimental apparatus at these high oxygen partial pressures at temperatures below 1300 °C; thus, they have been excluded from the data set. The perovskites display steeper isotherms than ceria across the entire oxygen partial pressure range at equivalent temperatures as well as much deeper reduction extents. LSMG6482, in particular, experienced significant $\Delta\delta$ across the low-temperature isotherms (1200 and 1250 °C) compared to its aluminum-doped analogue, LSMA6482. At higher temperatures, the perovskites experienced similar $\Delta\delta$ values, with LSMG6482 being marginally larger. For example, at 1400 °C, the $\Delta\delta$ across the entire oxygen partial pressure range in order from lowest to highest was 0.009, 0.027, 0.036, 0.035, and then 0.037 for ceria, LSMA6446, LSMA6482, LSMA6464, and then LSMG6482, respectively. Interestingly, LSMG6482 appears more sensitive to temperature change at constant pO₂ than the Al-doped perovskites. Specifically, at a pO₂ of 10^{-3.94} atm, LSMG6482 experiences a $\Delta\delta$ of 0.07 from 1200 to 1400 °C. At this same condition, LSMA6446, LSMA6464, and LSMA6482 saw a $\Delta\delta$ of 0.051, 0.052, and 0.055, respectively. The values for ceria are in excellent agreement with accepted values reported in the literature.⁶ The values for the aluminum-doped perovskites generally agree well with predictions made with thermodynamic data from Ebziri et al. and Takacs et al. for LSMA6482 and LSMA6446, with some deviation at 1400 °C.^{17,18} Results for LSMA6464 are in excellent agreement with predictions at lower temperatures but deviate significantly at temperatures above 1300 °C. This could be caused by a difference in secondary phase growth, discussed in a later section, though postcycling characterization is not reported by the related literature. A comparison of equilibrium values to the literature for each material can be found in Figure S1. Direct comparisons to Dey et al. could not be made for LSMG because the A-site concentrations of Sr are different and their pO₂ is not reported; however, the results are qualitatively consistent where when holding doping concentrations constant, the Ga sample reduces further than the Al sample.²⁴

Thermodynamic properties, namely, partial molar enthalpy ($\Delta\bar{h}_o$) and entropy ($\Delta\bar{s}_o$) as a function of δ , were calculated for each material as a function of δ based on the data presented in Figure 2 (see Figure S3). Our calculations (methodology described in Figure S2) show that B-site doping with Ga on the LSM system results in an increase in the thermodynamic properties compared with doping with Al with similar concentrations. For example, at a δ of 0.05, the determined $\Delta\bar{h}_o$ for LSMG6482 was 264.6 kJ mol⁻¹. This value is greater than that of its direct Al-doped analogue LSMA6482 with $\Delta\bar{h}_o$ of 208.5 kJ mol⁻¹ and comparable to that of LSMA6464 and

LSMA6446 with $\Delta\bar{h}_o$ of 272.4 and 263.4 kJ mol⁻¹, respectively. Similar trends can be seen for $\Delta\bar{s}_o$. Values for ceria and LSMA thermodynamic properties generally agree well with previously accepted studies.^{17,19}

Water Splitting Capability. The different ceramic compounds were subjected to three water splitting cycles in the SNL SFR to evaluate the water splitting capability of each material in terms of the H₂ yield and reversibility. Figure 3a

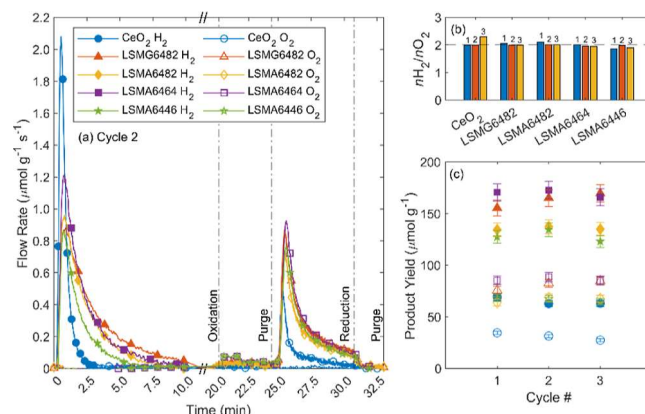


Figure 3. (a) Cycle 2 of three water splitting cycles performed in the SNL SFR. Hydrogen rate curves are shown with solid markers. Oxygen evolution rate curves are shown as open markers. (b) Ratio of moles of hydrogen produced to moles of oxygen evolved from the sample during cycles 1, 2, and 3. Perfect closure of the mass balance is marked by a dashed line at a value of 2. (c) Product yields, the integration of rate curves, shown with markers corresponding to plot (a) for hydrogen and oxygen. Oxidation occurred at 1200 °C, while reduction occurred at 1400 °C.

shows oxidation rates and reduction rates in terms of mass normalized hydrogen production rate and oxygen evolution rate during the second of three cycles repeated under the same conditions. Rate curves for all three cycles can be found in Figure S6. Similar data were obtained when varying the Ga doping concentration for the LSMG material, and the results are shown in Figures S8 through S10. Of the Ga-doping concentrations investigated, LSMG6482 produced the most H₂ and is compared to the Al-doped concentrations here. As shown in Figure 3a, ceria exhibited nearly double the peak oxidation rate compared to each perovskite and came to equilibrium within 3 min, while the perovskites took up to 10 min. However, the H₂ and O₂ yields of all perovskites were greater than those of ceria, as summarized in Figure 3c (mass-specific H₂ yield). Mole-specific H₂ yields are tabulated in the Supporting Information and follow the same trends. Importantly, each material exemplified excellent reversibility during water splitting. This is shown in Figure 3b, where the molar H₂ to O₂ ratio is equal to or near 2 for each cycle. In general, LSMA6464 and LSMG6482 H₂ yields during the second cycle were similar (172.8 and 165.1 $\mu\text{mol g}^{-1}$, respectively). LSMA6482 and LSMA6446 had lower yields of 137.4 and 134.5 $\mu\text{mol g}^{-1}$, respectively, and ceria produced the lowest yield of 62.9 $\mu\text{mol g}^{-1}$. Peak perovskite oxidation rates were similar among all perovskites at approximately 0.9 $\mu\text{mol g}^{-1} \text{s}^{-1}$ except for LSMA6464, which peaked at 1.2 $\mu\text{mol g}^{-1} \text{s}^{-1}$. Perovskite reduction rates were similar, with the peak rate decreasing slightly from 0.93 to 0.87, 0.77, and 0.73 for LSMA6464, LSMG6482, LSMA6446, and LSMA6482, re-

spectively. While generally, the perovskites produced significantly more H₂ per unit mass than ceria under these conditions, the advantage of faster oxidation rates when using ceria may be of advantage when considering more optimized cycle timing to maximize time-averaged H₂ output, not cycling to equilibrium. For all materials considered, the molar ratio of H₂ to O₂ was approximately 2, demonstrating the ability of each material to reversibly split H₂O in a thermochemical cycle. For this analysis, thermolysis and apparatus effects were accounted for by blank subtraction. Rates before blank subtraction can be found in Figures S6 and S8. However, note that there was some existing equilibrium hydrogen production at the end of each oxidation. This is understood to be thermolysis on the surface of the sample. The steady rate was assumed constant and subtracted from the integration for reporting yield and closing the mass balance. Therefore, each H₂ rate curve in Figure 3a has been shifted down slightly such that the steady-state production rate is 0 at equilibrium. Reported yields have an uncertainty of $\pm 4.9\%$ based on the mass balance of the data presented (details in Supporting Information). A comparison of the experimental yields measured here for each of the three cycles is presented in Table S3 in terms of $\Delta\delta$ to predictions for yield if materials were given sufficient time to equilibrate, based on thermodynamic data from Panlener et al. for ceria, Ezbiri et al. for the LSMA materials, and the presently calculated values for LSMG.^{6,17} Compared to predictions, these cycles access an average of 25, 31, 18, 22, and 27% of the estimated yields for ceria, LSMG6482, LSMA6482, LSMA6464, and LSMA6446, respectively, likely due to incomplete reductions during the allotted time of reaction seen in Figure 3a. Further, in Table S4, the utilization extent of these cycles is analyzed, that is, the measured yield as a fraction of the yield assuming the materials are given sufficient time to reduce and are capable of fully reoxidizing to $\delta = 0$ under different conditions (i.e., a large temperature swing and sufficient time). The average utilization extent across the three cycles is 23, 22, 15, 16, and 15% for ceria, LSMG6482, LSMA6482, LSMA6464, and LSMA6446, respectively.

Further insights into each material's water splitting capability can be gathered from a comparison of steam conversion, shown in Figure 4. Conversion as a function of time is defined mathematically in eq 4.

$$X_{H_2O} = \frac{\int_{t_0}^t \dot{n}H_2_{\text{produced}}(t) dt}{\int_{t_0}^t \dot{n}H_2O_{\text{delivered}}(t) dt} \times 100\% \quad (4)$$

The peak conversion achieved during each cycle (where eq 4 is maximized) is compared for each material (solid bars) as well as the final steam conversion achieved at the end of the reaction (hatch-marked bars). It should be noted that quantitatively, these values are exaggeratedly low as the SFR and the experimental conditions are not optimized for quantifying steam conversion; however, a comparison can be made between materials under these controlled conditions. Mass-specific H₂ yield at the point of peak conversion is also shown as green circles, corresponding to the right axis, for each cycle and each material. It is apparent that ceria, at its peak, converts nearly double the input steam compared to the perovskites under their peak conditions for similar H₂ production. Under the constant unoptimized steam flow rate experienced by each material, this is a direct result of a

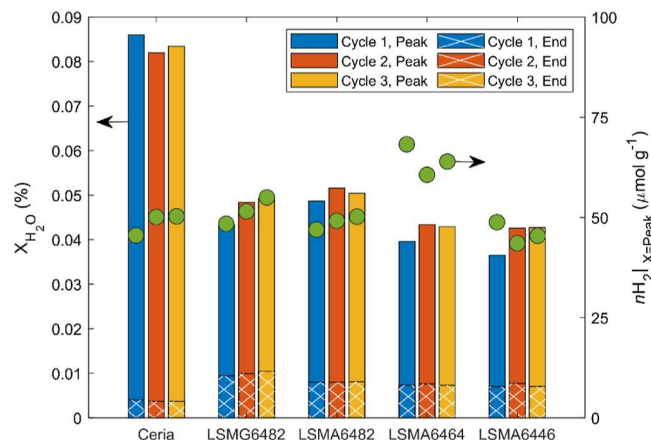


Figure 4. Peak steam conversion (colored bars) and corresponding H₂ yield (green circles) achieved during each water splitting cycle and final steam conversion at the end of the 1300 s reaction (hatch-marked bars).

difference in oxidation kinetics. However, over the entire oxidation period, Ga- and Al-doped perovskites convert more steam because of their deeper reduction extent.

High Conversion Water Splitting. Results for high conversion water splitting are summarized in Figures 5 and 6. Figure 5 shows the oxidation rates of each material, while Figure 6 shows the corresponding hydrogen yields and mass balance. Together, these results can be used to gain an understanding of how well each material can split water or rather how much excess steam must be supplied in order to reverse the reduction reaction. In Figure 5, it is shown that for all materials at each condition, increasing the nH₂O/nH₂ ratio, or R, during oxidation results in both larger peak H₂ production rates and larger total H₂ yields. Rates also increase with increasing temperature, most notably so with ceria as potential for reoxidation increases with increasing temperature. At these conditions, the LSMA6464 peak H₂ production rate is consistently higher than that of each of the other materials. Rate curves from Figure 5 were integrated with time to obtain the mass specific H₂ yields during each oxidation, presented in Figure 6. Mole-specific H₂ yields are tabulated in the Supporting Information and follow the same trends.

Each perovskite consistently produced more H₂ than ceria except for LSMA6446 at the highest temperature. In general, the perovskite ordering of the total H₂ yield at each condition from highest to lowest was LSMG6482, LSMA6482, LSMA6464, and then LSMA6446. The latter two materials are in qualitative agreement with water splitting yields measured by McDaniel et al.¹² At 1400 °C, LSMA6482 produced marginally more H₂ than LSMG6482 under each oxidation condition, though the differences are within the assigned error. This deviates from findings from Dey et al. where Ga doped compositions produced 38% more H₂ compared to Al at equivalent doping concentrations, albeit at significantly different reaction conditions and doping concentrations from those seen here. Steam conversion during each oxidation can be seen in Figure S11. In general, trends in conversion at these conditions are similar among LSMG6482, LSMA6482, and LSMA6464, all of which are slightly greater in magnitude at each condition than LSMA6446. Similar to trends seen in Figure 6, ceria suffers in conversion at 1300 °C due to thermodynamic limitations but becomes more comparable to the perovskites as the temperature is increased,

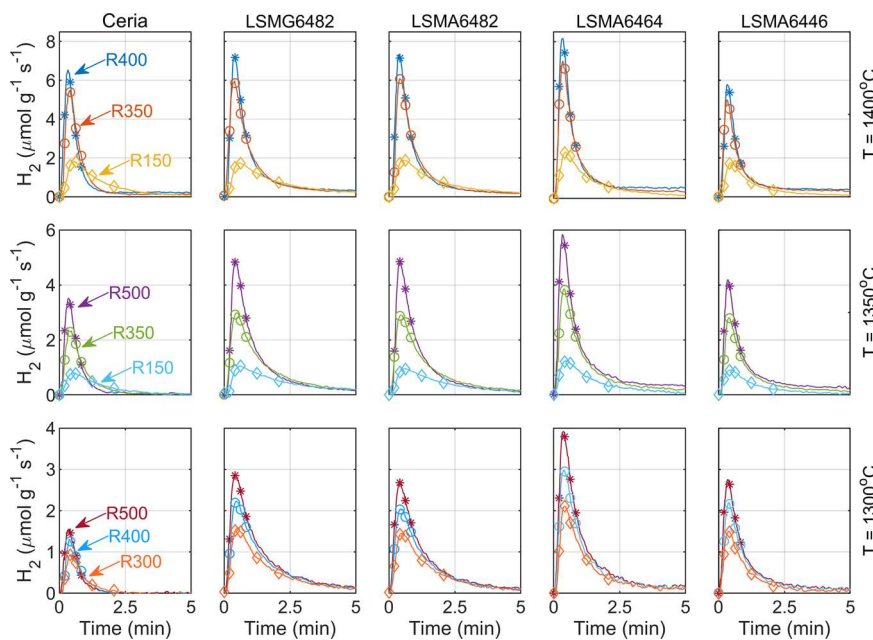


Figure 5. Oxidation rates during high conversion water splitting experiments for each material (columns) at three different temperatures (rows). $[nH_2O/nH_2]$ ratios (R) are labeled for each temperature in the ceria column, where asterisk markers denote the highest ratio followed by circles and then diamonds. Each reduction took place at $10^{-6.5}$ atm.

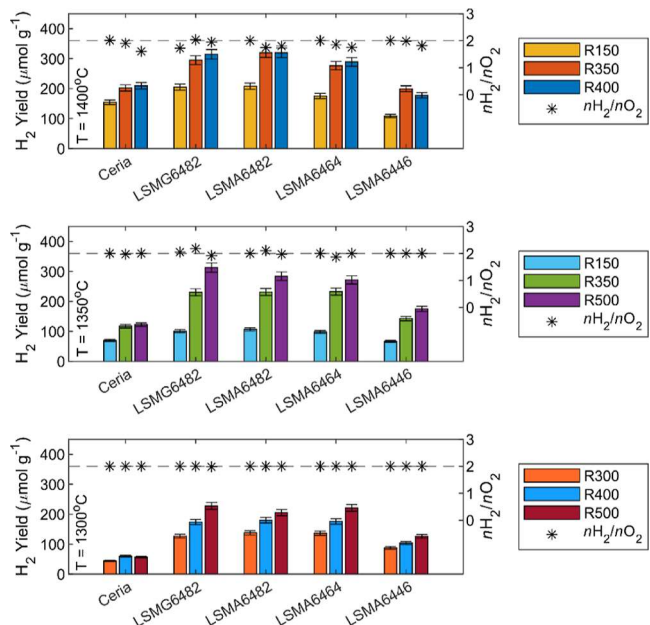


Figure 6. Mass-specific hydrogen yields (bars) and mass balance (asterisks) for each oxidation under controlled nH_2O/nH_2 , here labeled R , for temperatures 1300, 1350, and 1400 °C.

surpassing the conversion metrics of LSMA6446 at 1400 °C. As was done in the prior analysis of Figure 3, steady-state hydrogen production rates were subtracted to close the mass balance. The effect becomes more prevalent as the temperature and steam-to-hydrogen ratio is increased. This is reflected in the scatter of the mass balance seen in each plot of Figure 6. Error bars of $\pm 5.3\%$ are shown on each bar based on the mass balance of the data presented (details in Supporting Information).

Insights into how the perovskites perform relative to ceria at these conditions can be gained from Figure 7. Here, H_2 yields

T (°C)	nH_2O/nH_2	$nH_2_{LSMG6482}/nH_2_{ceria}$	$nH_2_{LSMA6482}/nH_2_{ceria}$	$nH_2_{LSMA6464}/nH_2_{ceria}$	$nH_2_{LSMA6446}/nH_2_{ceria}$
1400	150	1.3	1.4	1.1	0.7
	350	1.5	1.6	1.4	1
	400	1.5	1.5	1.4	0.8
1350	150	1.5	1.5	1.4	1
	350	2.0	2.0	2.0	1.2
	500	2.6	2.3	2.2	1.4
1300	300	2.9	3.1	3.1	2
	400	2.9	3.0	2.9	1.7
	500	4.0	3.6	3.9	2.2

Figure 7. Mass-specific H_2 yield for each perovskite normalized to the mass-specific H_2 yield of ceria at each condition.

for each perovskite were normalized to that of ceria. This demonstrates the trade-off that comes with perovskite operation when compared to ceria. That is, the perovskites must oxidize at higher ratios (R) of steam to hydrogen (i.e., excess steam conditions) in order to achieve significantly larger hydrogen yields than ceria. When oxidizing at low ratios, for example R150, the perovskites do not have as much advantage—but still generally outperform ceria by 30–60% in the case of LSMG6482 and LSMA6482. This can be seen by observing the normalized yields in Figure 7 at 1350 °C. As the ratio increases, the perovskites perform better, with LSMG6482 producing increasingly more hydrogen than ceria, from 1.5× at R150 to 2.6× at R500. This trend can generally be observed at all three temperature conditions. The divergence in the H_2 yield between ceria and the perovskites as R is increased is qualitatively consistent with those of McCord et al.³⁰ An additional advantage of the perovskites that can be observed from Figure 7 is their operability at lower temperatures. At 1300 °C and R500, though total H_2 yields are lower than at the higher temperature conditions, LSMG6482 produced the maximum of 4× the amount of H_2 as ceria with the other perovskites producing between 2.2× and 3.9× depending on doping concentrations. At these conditions, the deep reduction extents of each perovskite become beneficial when compared to that of ceria as they retain significant potential for reoxidation as excess steam is introduced, whereas ceria begins to approach full reoxidation.

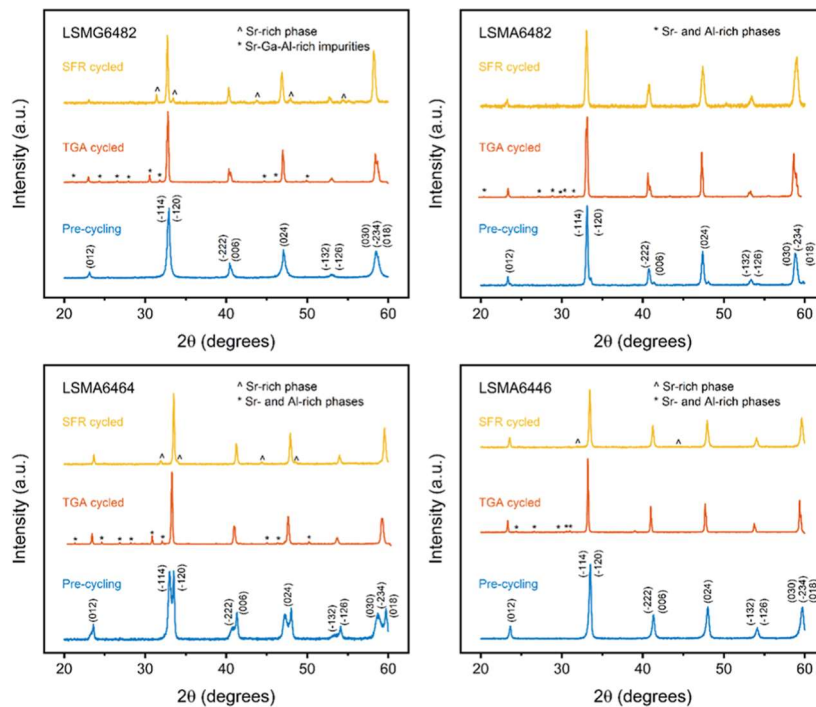


Figure 8. XRD patterns for perovskites precycling, post-TGA, and post-SFR.

Crystallographic Phase Analysis. The XRD patterns for the samples prior to and after cycling in each system are listed in Figure 8. While undoped LaMnO_3 generally forms in the orthorhombic structure depending on the processing methods, the addition of Sr to the A-site results in a rhombohedral structure in the $R\bar{3}c$ space group for 40% substitution of Sr on the A-site.^{31,32} Therefore, the expected structure of all doped materials shown here is expected to be the $R\bar{3}c$ space group due to the Sr content and Mn^{4+} . The precycled materials are all observed to have the $R\bar{3}c$ space group with no secondary phases. All samples were also investigated after TGA and SFR cycling to investigate the compositional changes that occur in the materials from redox cycling. Prior X-ray photoelectron spectroscopy (XPS) experiments and literature of LSM redox cycling have shown that Sr segregates to the surface of the material at high temperatures.³³ Therefore, if secondary phases are observed, then it is expected that these phases will be Sr rich.

After TGA and SFR cycling of LSMG6482, secondary phases are observed in both samples; however, different secondary phases are observed. Based on our ongoing XPS studies and prior work in the literature, a Sr-rich secondary phase is expected. Additionally, the formation of a spinel phase is the most likely reaction species to occur. Moreover, a spinel-type phase is most likely formed based on phase equilibria work by Cherepanov that found that LSM may decompose into $(\text{La}_{1-x}\text{Sr}_x)_2\text{MnO}_{4-\delta}$ at low $p\text{O}_2$.³⁴ Energy-dispersive spectrometry (EDS) mapping and scanning electron microscopy (SEM) with backscatter electrons (BSE) did not reveal appreciable contrast for the identification of a secondary phase following SFR cycling, even though the phase appears to account for ~15% of the material based on XRD. EDS mapping and SEM with BSE of the LSMG6482 powder following SFR cycling can be found in Figures S12 and S13, respectively. After TGA cycling, a significantly larger percentage of secondary phase appears for the LSMG6482

sample compared to only 7% for LSMA6464 and 4% for LSMA6446, owing to the reactivity of Ga compared to that of Al. The TGA cycled sample showed significant BSE contrast between secondary and primary phases. EDS analysis of the secondary phase showed it to be Sr-Ga rich. Additionally, small Al impurities were identified in the material, likely a result of the reactor setup with a highly reactive nature of the material.

The LSMA6464 and LSMA6446 samples after SFR cycling display a secondary phase similar to that of the LSMG6482 sample but with a slight shift to higher 2θ values. No secondary phases were observed in the LSMA6482 sample. Based on the analysis of the LSMG6482 sample, this is likely a Sr- and Al-rich spinel. The replacement of Ga with Al would explain the shift to higher 2θ values due to the smaller ionic radius of Al. Similar to the case for the LSMG6482 sample, no appreciable contrast was observed with EDS and BSE to further identify the secondary phase. Secondary phases, however, were observed in the TGA samples. An overall enrichment of Sr and depletion of Mn while the La content stayed consistent was observed for the bulk sample. All identified secondary phases in the LSMA6482, LSMA6464, and LSMA6446 samples are Sr- and Al-rich. EDS analysis of the LSMA6446 TGA cycled sample is included in Figure S14 for reference.

Discussion on Stability. The above crystallographic phase analysis notes the growth of Sr- and Al-rich secondary phases after cycling in both the TGA pellets (i.e., lower reduction extents and higher $p\text{O}_2$) and the SFR powder samples (i.e., higher reduction extents and lower $p\text{O}_2$). However, this phase growth did not result in an observable decrease in oxygen exchange capacity during experimentation. For example, the repeatability of the TGA results presented in Figure 1 can be gauged from the vertical error bars in Figure 2, which represent two standard deviations from the average of each equilibrium point based on the sample of data collected at that condition. In total, the two different samples used for these experiments

were each cycled over 40 times to obtain the equilibrium points shown in Figure 2. To probe the stability under repeatable redox conditions, the 200 μm LSMG6482 pellet was cycled another 10 times following characterization in the TGA. The results are shown in Figure S15. The top subplot shows a representative TGA experiment as the temperature and $p\text{O}_2$ are varied. The middle subplot shows the 10 repeatable cycles. The bottom subplot shows nonstoichiometry for these 10 cycles and 2 cycles extracted from the top subplot under the same temperature and $p\text{O}_2$ conditions. In total, the data presented occur over 50 h of cycling time, with no obvious changes in bulk oxygen capacity. Further, SFR experiments showed no decreasing trend in H_2 yield in the three laser-driven cycles for any material, and no sign of deactivation in the nine following high conversion cycles. While these trends lend confidence toward the short-term stability of the doped LSM materials, the long-term stability of these materials should be further studied in future studies to better estimate stability over longer durations. For example, according to Ma et al., the typical lifetime of a redox material should be on the order of 10 cycles per day for 10 years or greater to ensure economic viability.³⁵

CONCLUSIONS

In this study, Ga-doped LSM-type perovskite, identified through DFT calculations of E_v^{O} as a potential water splitting metal oxide for thermochemical hydrogen production, was synthesized via solid-state synthesis as LSMG6482 alongside ceria, LSMA6482, LSMA6464, and LSMA6446 used for comparison.

TGA analysis revealed desirable redox behavior in LSMG6482 under high $p\text{O}_2$ conditions. LSMG6482 experienced greater changes in δ across $10^{-3.94}$ and $10^{-2.94}$ atm than the aluminum-doped materials in addition to operating at a deeper reduction extent than all materials except LSMA6446. This is important when operation is expected to occur with high oxidation temperatures because increased sensitivity to $p\text{O}_2$ changes lead to increased H_2 yield with little additional oxidant input. Further, the ability to operate at deeper reduction extents allows for potential operation at lower temperatures as well as avoiding limited reoxidation (i.e., reoxidation to $\delta = 0$). During temperature swing water splitting, LSMG6482 was shown to reversibly split water, in a similar capacity as LSMA6464, yielding 2.62 times as much H_2 compared to ceria. During high conversion experiments, it was shown that LSMG6482 and the other perovskites produce up to 314 $\mu\text{mol H}_2 \text{ g}^{-1}$ when oxidizing at high temperatures and higher ratios (i.e., low conversion with excess steam). At lower temperatures with excess steam, LSMG6482 produced 4× the amount of H_2 when compared to ceria. However, when oxidizing at lower ratios (i.e., high conversion conditions) and high temperatures, the perovskites performed only marginally better than ceria. Steam conversion was quantified during both temperature swing experiments, with perovskite steam conversions of ~0.05%, and high conversion experiments, with conversions ranging between roughly 0.1 and 0.5%. While these conversions were quantified in an unoptimized reactor and conditions not suitable for maximizing steam conversion, the low magnitude does indicate a possible efficiency limitation due to long oxidation times that may be improved upon by advanced structural design such as the development of high-surface-area porous structures and optimized operating conditions. Secondary phase growth was detected in

LSMG6482, LSMA6464, and LSMA6446 after TGA and SFR cycling and in LSMA6482 after TGA cycling. TGA resulted in the growth of Sr- and Al/Ga-rich phases, while SFR resulted in growth of Sr- and Al/Ga-rich spinel phases.

Overall, the work presented herein has shown LSMG6482 to be a promising candidate for STCH production via water splitting redox cycles. Forthcoming investigations will include the characterization of redox stability over time, extension of equilibrium mapping into lower $p\text{O}_2$, and modeling the water splitting behavior of LSMG6482. Further, the solar-to-fuel efficiency of LSMG6482 should be measured in a reactor optimized for high conversions and minimal heat loss.

ASSOCIATED CONTENT

Supporting Information

The Supporting Information is available free of charge at <https://pubs.acs.org/doi/10.1021/acs.jpcc.4c02797>.

Comparison of the experimental results to the theoretical predictions and utilization extents; H_2 yields normalized to moles of oxide; partial molar thermodynamic properties of metal oxides; SFR product quantification and calibration details; full-scale experimental results from the SFR before/after blank subtraction; Ga-doped LSM compositional variation H_2 production; steam conversion details from high conversion experiments; postcycling characterization details; LSMG6482 stability demonstration; and uncertainty details ([PDF](#))

AUTHOR INFORMATION

Corresponding Author

Jonathan R. Scheffe — Department of Mechanical and Aerospace Engineering, University of Florida, Gainesville, Florida 32611, United States; Email: jscheffe@ufl.edu

Authors

Dylan C. McCord — Department of Mechanical and Aerospace Engineering, University of Florida, Gainesville, Florida 32611, United States; orcid.org/0000-0002-6083-1354

Elizabeth J. Gager — Department of Materials Science and Engineering, University of Florida, Gainesville, Florida 32611, United States

Ximeng Wang — Department of Materials Science and Engineering, University of Florida, Gainesville, Florida 32611, United States; orcid.org/0000-0002-3943-7184

Taylor L. Johnson — Department of Mechanical and Aerospace Engineering, University of Florida, Gainesville, Florida 32611, United States

Jonas S. Beachy — Department of Mechanical and Aerospace Engineering, University of Florida, Gainesville, Florida 32611, United States

Keith A. King — Sandia National Laboratories, Livermore, California 94550, United States

Simon R. Phillpot — Department of Materials Science and Engineering, University of Florida, Gainesville, Florida 32611, United States; orcid.org/0000-0002-7774-6535

Juan C. Nino — Department of Materials Science and Engineering, University of Florida, Gainesville, Florida 32611, United States

Anthony H. McDaniel — Sandia National Laboratories, Livermore, California 94550, United States

Complete contact information is available at:
<https://pubs.acs.org/10.1021/acs.jpcc.4c02797>

Notes

The authors declare no competing financial interest.

ACKNOWLEDGMENTS

We gratefully acknowledge financial support from the U.S. Department of Energy Hydrogen and Fuel Cell Technologies Office (award number: EE0008840), the U.S. Department of Energy Solar Energy Technologies Office (award number: EE00010315), and the NSF REU program (site: Engineering for Healthcare). Sandia National Laboratories is a multimission laboratory managed and operated by National Technology & Engineering Solutions of Sandia, LLC (NTESS), a wholly owned subsidiary of Honeywell International Inc., for the U.S. Department of Energy's National Nuclear Security Administration (DOE/NNSA) under contract DE-NA0003525. This written work is authored by an employee of NTESS. The employee, not NTESS, owns the right, title, and interest in and to the written work and is responsible for its contents. Any subjective views or opinions that might be expressed in the written work do not necessarily represent the views of the U.S. Government. The publisher acknowledges that the U.S. Government retains a nonexclusive, paid-up, irrevocable, worldwide license to publish or reproduce the published form of this written work or allow others to do so, for U.S. Government purposes. The DOE will provide public access to results of federally sponsored research in accordance with the DOE Public Access Plan.

REFERENCES

- (1) Carrillo, R. J.; Scheffe, J. R. Beyond Ceria: Theoretical Investigation of Isothermal and Near Isothermal Redox Cycling of Perovskites for Solar Thermochemical Fuel Production. *Energy Fuels* **2019**, *33* (12), 12871–12884.
- (2) Chueh, W.; Falter, C.; Abbott, M.; Scipio, D.; Furley, P.; Haile, S.; Steinfeld, A. High-Flux Solar-Driven Thermochemical Dissociation of CO₂ and H₂O Using Nonstoichiometric Ceria. *Science* **2010**, *330*, 1797–1801.
- (3) Chueh, W. C.; Haile, S. M. A thermochemical study of ceria: exploiting an old material for new modes of energy conversion and CO₂ mitigation. *Philos. Trans. R. Soc., A* **2010**, *368* (1923), 3269–3294.
- (4) Scheffe, J. R.; Steinfeld, A. Thermodynamic Analysis of Cerium-Based Oxides for Solar Thermochemical Fuel Production. *Energy Fuels* **2012**, *26* (3), 1928–1936.
- (5) Ackermann, S.; Scheffe, J. R.; Steinfeld, A. Diffusion of oxygen in ceria at elevated temperatures and its application to H₂O/CO₂ splitting thermochemical redox cycles. *J. Phys. Chem. C* **2014**, *118* (10), 5216–5225.
- (6) Panlener, R. J.; Blumenthal, R. N.; Garnier, J. E. A thermodynamic study of nonstoichiometric cerium dioxide. *J. Phys. Chem. Solids* **1975**, *36* (11), 1213–1222.
- (7) Siegrist, S.; von Storch, H.; Roeb, M.; Sattler, C. Moving brick receiver-reactor: a solar thermochemical reactor and process design with a solid–solid heat exchanger and on-demand production of hydrogen and/or carbon monoxide. *J. Sol. Energy Eng.* **2019**, *141* (2), 021009.
- (8) Marxer, D.; Furley, P.; Takacs, M.; Steinfeld, A. Solar thermochemical splitting of CO₂ into separate streams of CO and O₂ with high selectivity, stability, conversion, and efficiency. *Energy Environ. Sci.* **2017**, *10* (5), 1142–1149.
- (9) Zoller, S. A 50 kW Solar Thermochemical Reactor for Syngas Production Utilizing Porous Ceria Structures; ETH Zurich, 2020.
- (10) Kubicek, M.; Bork, A. H.; Rupp, J. L. M. Perovskite oxides – a review on a versatile material class for solar-to-fuel conversion processes. *J. Mater. Chem. A* **2017**, *5* (24), 11983–12000.
- (11) Scheffe, J. R.; Weibel, D.; Steinfeld, A. Lanthanum–Strontium–Manganese Perovskites as Redox Materials for Solar Thermochemical Splitting of H₂O and CO₂. *Energy Fuels* **2013**, *27* (8), 4250–4257.
- (12) McDaniel, A. H.; Miller, E. C.; Arifin, D.; Ambrosini, A.; Coker, E. N.; O’Hayre, R.; Chueh, W. C.; Tong, J. Sr-and Mn-doped LaAlO₃–δ for solar thermochemical H₂ and CO production. *Energy Environ. Sci.* **2013**, *6* (8), 2424–2428.
- (13) McDaniel, A. H.; Ambrosini, A.; Coker, E. N.; Miller, J. E.; Chueh, W. C.; O’Hayre, R.; Tong, J. Nonstoichiometric perovskite oxides for solar thermochemical H₂ and CO production. *Energy Procedia* **2014**, *49*, 2009–2018.
- (14) Ezbiri, M.; Becattini, V.; Hoes, M.; Michalsky, R.; Steinfeld, A. High Redox Capacity of Al-Doped La_xSr_yMnO_δ Perovskites for Splitting CO₂ and H₂O at Mn-Enriched Surfaces. *ChemSusChem* **2017**, *10* (7), 1517–1525.
- (15) Şanlı, S. B.; Pişkin, B. Effect of B-site Al substitution on hydrogen production of La0.4Sr0.6Mn1-xAlx (x= 0.4, 0.5 and 0.6) perovskite oxides. *Int. J. Hydrogen Energy* **2022**, *47* (45), 19411–19421.
- (16) Deml, A. M.; Stevanović, V.; Holder, A. M.; Sanders, M.; O’Hayre, R.; Musgrave, C. B. Tunable Oxygen Vacancy Formation Energetics in the Complex Perovskite Oxide Sr_xLa_xMn_yAl_yO₃. *Chem. Mater.* **2014**, *26* (22), 6595–6602.
- (17) Ezbiri, M.; Takacs, M.; Theiler, D.; Michalsky, R.; Steinfeld, A. Tunable thermodynamic activity of LaxSr1-xMnyAl1-yO3-δ (0 ≤ x ≤ 1, 0 ≤ y ≤ 1) perovskites for solar thermochemical fuel synthesis. *J. Mater. Chem. A* **2017**, *5* (8), 4172–4182.
- (18) Takacs, M.; Hoes, M.; Caduff, M.; Cooper, T.; Scheffe, J. R.; Steinfeld, A. Oxygen nonstoichiometry, defect equilibria, and thermodynamic characterization of LaMnO₃ perovskites with Ca/Sr A-site and Al B-site doping. *Acta Mater.* **2016**, *103*, 700–710.
- (19) Cooper, T.; Scheffe, J. R.; Galvez, M. E.; Jacot, R.; Patzke, G.; Steinfeld, A. Lanthanum Manganite Perovskites with Ca/Sr A-site and Al B-site Doping as Effective Oxygen Exchange Materials for Solar Thermochemical Fuel Production. *Energy Technol.* **2015**, *3* (11), 1130–1142.
- (20) Muhich, C. L.; Blaser, S.; Hoes, M. C.; Steinfeld, A. Comparing the solar-to-fuel energy conversion efficiency of ceria and perovskite based thermochemical redox cycles for splitting H₂O and CO₂. *Int. J. Hydrogen Energy* **2018**, *43* (41), 18814–18831.
- (21) Lee, K.; McCord, D. C.; Carrillo, R. J.; Guyll, B.; Scheffe, J. R. Improved Performance and Efficiency of Lanthanum–Strontium–Manganese Perovskites Undergoing Isothermal Redox Cycling under Controlled pH₂O/pH₂. *Energy Fuels* **2020**, *34* (12), 16918–16926.
- (22) Muhich, C. L.; Evanko, B. W.; Weston, K. C.; Lichy, P.; Liang, X.; Martinek, J.; Musgrave, C. B.; Weimer, A. W. Efficient generation of H₂ by splitting water with an isothermal redox cycle. *Science* **2013**, *341* (6145), 540–542.
- (23) Hao, Y.; Yang, C.-K.; Haile, S. M. High-temperature isothermal chemical cycling for solar-driven fuel production. *Phys. Chem. Chem. Phys.* **2013**, *15* (40), 17084–17092.
- (24) Dey, S.; Naidu, B. S.; Rao, C. N. R. Beneficial effects of substituting trivalent ions in the B-site of La0.5Sr0.5Mn1-xAxO₃ (A = Al, Ga, Sc) on the thermochemical generation of CO and H₂ from CO₂ and H₂O. *Dalton Trans.* **2016**, *45* (6), 2430–2435.
- (25) Liu, C.; Zhang, D.; Li, W.; Trindell, J. A.; King, K. A.; Bishop, S. R.; Sugar, J. D.; McDaniel, A. H.; Smith, A. I.; Salinas, P. A.; et al. Manganese-based A-site high-entropy perovskite oxide for solar thermochemical hydrogen production. *J. Mater. Chem. A* **2024**, *12* (7), 3910–3922.
- (26) Emery, A. A.; Saal, J. E.; Kirklin, S.; Hegde, V. I.; Wolverton, C. High-Throughput Computational Screening of Perovskites for Thermochemical Water Splitting Applications. *Chem. Mater.* **2016**, *28* (16), 5621–5634.
- (27) McDaniel, A. H.; Allendorf, M. D.; Scheffe, J. R.; Weimer, A. W. Kinetics and Mechanism of solar-thermochemical H₂ production by

oxidation of a cobalt ferrite-zirconia composite; Sandia National Laboratories (SNL): Albuquerque, NM, and Livermore, CA, 2012.

(28) Arifin, D.; Aston, V. J.; Liang, X.; McDaniel, A. H.; Weimer, A. W. CoFe₂O₄ on a porous Al₂O₃ nanostructure for solar thermochemical CO₂ splitting. *Energy Environ. Sci.* **2012**, *5* (11), 9438–9443.

(29) Wang, X.; Goyal, A.; Zhou, P.; Gager, E.; McCord, D.; Nino, J. C.; Scheffe, J. R.; Lany, S.; Phillipot, S. R. LaMnO₃ Dopants for Efficient Thermochemical Water Splitting Identified by Density Functional Theory Calculations. *J. Phys. Chem. C* **2023**, *127* (49), 23988–24000.

(30) McCord, D.; Gager, E. J.; Lee, K.; McDaniel, A.; Nino, J. C.; Scheffe, J. Assessment of Bulk Oxygen Capacity and Transient Redox Behavior of Foamed Lanthanum Strontium Manganese Perovskites. *J. Sol. Energy Eng.* **2023**, *146*, 021005–1.

(31) Takeda, Y.; Nakai, S.; Kojima, T.; Kanno, R.; Imanishi, N.; Shen, G. Q.; Yamamoto, O.; Mori, M.; Asakawa, C.; Abe, T. Phase relation in the system (La_{1-x}A_x)_{1-y}MnO_{3+z} (A= Sr and Ca). *Mater. Res. Bull.* **1991**, *26* (2–3), 153–162.

(32) Rørmark, L.; Wiik, K.; Stølen, S.; Grande, T. Oxygen stoichiometry and structural properties of La_{1-x}A_xMnO_{3±δ} (A= Ca or Sr and 0≤ x≤ 1). *J. Mater. Chem.* **2002**, *12* (4), 1058–1067.

(33) Koo, B.; Kim, K.; Kim, J. K.; Kwon, H.; Han, J. W.; Jung, W. Sr segregation in perovskite oxides: why it happens and how it exists. *Joule* **2018**, *2* (8), 1476–1499.

(34) Cherepanov, V.; Barkhatova, L. Y.; Voronin, V. Phase equilibria in the La–Sr–Mn–O system. *J. Solid State Chem.* **1997**, *134* (1), 38–44.

(35) Ma, Z.; Davenport, P.; Saur, G. System and technoeconomic analysis of solar thermochemical hydrogen production. *Renewable Energy* **2022**, *190*, 294–308.